The Astrophysical Journal, 692:309–323, 2009 February 10 doi:10.1088/0004-637X/692/1/309

SPATIALLY RESOLVED SPECTROSCOPY OF SUB–AU-SIZED REGIONS OF T TAURI AND HERBIG AE/BE DISKS

J. A. Eisner[1,2,3], J. R. Graham[2], R. L. Akeson[4], and J. Najita[5]
[1] Steward Observatory, University of Arizona, Tucson, AZ 85721, USA
[2] University of California at Berkeley, Department of Astronomy, 601 Campbell Hall, Berkeley, CA 94720, USA
[3] Miller Institute for Basic Research in Science, Berkeley, CA 94720, USA
[4] California Institute of Technology, Michelson Science Center MC 100-22, Pasadena, CA 91125, USA
[5] National Optical Astronomy Observatory, 950 N. Cherry Avenue, Tucson, AZ 85719, USA
Received 2008 June 22; accepted 2008 September 24; published 2009 February 19

ABSTRACT

We present spatially resolved near-IR spectroscopic observations of 15 young stars. Using a grism spectrometer behind the Keck interferometer, we obtained an angular resolution of a few milliarcseconds and a spectral resolution of 230, enabling probes of both gas and dust in the inner disks surrounding the target stars. We find that the angular size of the near-IR emission typically increases with wavelength, indicating hot, presumably gaseous material within the dust sublimation radius. Our data also clearly indicate Brγ emission arising from hot hydrogen gas, and suggest the presence of water vapor and carbon monoxide gas in the inner disks of several objects. This gaseous emission is more compact than the dust continuum emission in all cases. We construct simple physical models of the inner disk and fit them to our data to constrain the spatial distribution and temperature of dust and gas emission components.

Key words: circumstellar matter – stars: individual (AS 205, AS 442, DG Tau, MWC 275, MWC 480, MWC 758, MWC 863, MWC 1080, HD 141569, HD 142666, HD 144432, RY Tau, RW Aur, V1295 Aql, VV Ser) – stars: pre-main sequence – techniques: interferometric – techniques: spectroscopic

1. INTRODUCTION

Protoplanetary disks provide a reservoir of material from which planets may form, and the abundance and properties of extrasolar planets (e.g., Marcy et al. 2005), as well as the architecture of our own solar system, suggest that planets frequently form in or migrate through inner regions of protoplanetary disks. Furthermore, the innermost disk regions represent the interface between the inwardly accreting disk and the magnetized central star, and it is here that material accretes inward or is launched in winds or outflows (Shu et al. 1994). Knowledge of the distribution of material in the inner disk is therefore crucial for understanding the mass assembly and angular momentum evolution of pre-main-sequence stars.

Modeling of spectral energy distributions (e.g., Bertout et al. 1988; Lada & Adams 1992) and spectrally resolved gaseous emission lines (e.g., Najita et al. 1996a, 2007; Blake & Boogert 2004) provide important insights into the structure of protoplanetary disks in the terrestrial planet forming region. However, since these techniques typically rely on spectral information as a proxy for spatial information, they require assumptions about underlying geometric, temperature, or velocity structure. Recently, the technique of spectroastrometry, which capitalizes on the fact that emission centroids can be measured more precisely than the available angular resolution, has enabled less ambiguous constraints on disk structure (Pontoppidan et al. 2008). However, substantial gaps in our understanding remain due to a lack of high angular resolution observations.

Near-IR interferometry, which synthesizes a large aperture using two or more smaller, separated apertures, can achieve orders of magnitude higher angular resolution than conventional telescopes, and can spatially resolve disk terrestrial regions. For example, the Keck interferometer (KI), which combines the light from the two 10 m Keck apertures over an 85 m baseline, achieves a resolution approximately an order of magnitude higher than that attained with a single aperture. This means that angular scales of a few milliarcseconds, corresponding to a few tenths of an AU at typical distances to nearby star forming regions, can be spatially resolved with near-IR interferometers.

Most interferometric measurements to date have probed only the inner disk dust (e.g., Millan-Gabet et al. 2007, and references therein), which typically dominates the near-IR emission. To distinguish gas and dust, spectrally dispersed observations are required. Very few sources have been observed with spectrally dispersed interferometric observations to date (Eisner et al. 2007a; Eisner 2007; Malbet et al. 2007; Tatulli et al. 2007; Kraus et al. 2008; Isella et al. 2008). The observations showed intriguing evidence that gas and dust are not distributed uniformly in inner disk regions. Moreover, while observations of stars less massive than a few $M_{\odot}$ found gaseous emission to be more compact than dust emission (Eisner et al. 2007a; Eisner 2007), observations of the Brγ emission line around two more luminous stars found the gas to be more extended than the dust, presumably because the Brγ emission traces outflows from these young systems (Malbet et al. 2007; Tatulli et al. 2007). A larger sample is required to further investigate such potential trends, and to constrain the general properties of inner disk gas in young stars.

Here we present spectrally dispersed near-IR interferometry observations of a sample of young stars, including four T Tauri stars and 11 Herbig Ae/Be stars. Our data constrain the relative spatial and temperature distributions of dust and gas in sub–AU-sized regions of the disks around these stars.

2. OBSERVATIONS AND DATA REDUCTION

2.1. Sample

We selected a sample of young stars (Table 1) known to be surrounded by protoplanetary disks, all of which have been observed previously at near-IR wavelengths with long-baseline interferometers (Millan-Gabet et al. 2001; Eisner et al. 2004, 2005, 2007c; Colavita et al. 2003; Monnier et al. 2005; Akeson

Table 1
Target and Calibrator Properties

Source	α	δ	d	Spectral Type	m_V	m_K	References
			Target Stars				
RY Tau	04 21 57.409	+28 26 35.56	140	K1	10.2	5.4	1
DG Tau	04 27 04.700	+26 06 16.20	140	K3	12.4	7.0	2
MWC 480	04 58 46.266	+29 50 37.00	140	A2	7.7	5.5	3
RW Aur A	05 07 49.568	+ 30 24 05.161	140	K2	10.5	7.0	2
MWC 758	05 30 27.530	+25 19 57.08	140	A3	8.3	5.8	3
HD 141569	15 49 57.75	−03 55 16.4	99	B9/A0	7.1	6.7	3
HD 142666	15 56 40.023	−22 01 40.01	116	A8	8.8	6.1	4
HD 144432	16 06 57.957	−27 43 09.81	145	A9	8.2	5.9	4
AS 205 A	16 11 31.402	−18 38 24.54	160	K5	12.1	6.0	5
MWC 863 A	16 40 17.922	−23 53 45.18	150	A2	8.9	5.5	4
MWC 275	17 56 21.288	−21 57 21.88	122	A1	6.9	4.8	4
VV Ser	18 28 47.860	+00 08 40.00	310	A0	11.9	6.3	3
V1295 Aql	20 03 02.510	+05 44 16.68	290	B9/A0	7.8	5.9	3
AS 442	20 47 37.470	+43 47 24.90	600	B8	10.9	6.6	3
MWC 1080	23 17 25.574	+60 50 43.34	1000	B0	11.6	4.7	3
		Calibrator Stars					Applied to:
HD 27777	04 24 29.155	+34 07 50.73	187	B8V	5.7	6.0	RY Tau, MWC 480, MWC 758
HD 23642	03 47 29.453	+24 17 18.04	110	A0V	6.8	6.8	DG Tau, RW Aur
HD 23632	03 47 20.969	+23 48 12.05	120	A1V	7.0	7.0	DG Tau, RW Aur
HD 31464	04 57 06.426	+24 45 07.90	45	G5V	8.6	7.0	DG Tau, RW Aur
HD 139364	15 38 25.358	−19 54 47.45	53	F3V	6.7	5.7	HD 142666, HD 144432, AS 205 A
HD 141247	15 48 11.770	− 04 47 09.684	85	F9V	8.1	6.7	HD 141569
HD 143459	16 00 47.633	−08 24 40.87	141	A0Vs	5.5	5.5	HD 142666, HD 144432, AS 205 A
HD 145788	16 12 56.583	−04 13 14.912	171	A1V	6.3	6.2	HD 141569
HD 149013	16 32 38.133	−15 59 15.12	41	F8V	7.0	5.7	MWC 863
HD 163955	17 59 47.553	−23 48 58.08	134	B9V	4.7	4.9	MWC 275
HD 170657	18 31 18.960	−18 54 31.72	13	K1V	6.8	4.7	MWC 275
HD 183324	19 29 00.988	+01 57 01.61	59	A0V	5.8	5.8	V1295 Aql
HD 188385	19 54 40.200	+07 08 25.27	81	A2V	6.1	6.1	V1295 Aql
HD 199099	20 53 26.390	+42 24 36.72	138	A1V	6.7	6.7	AS 442, MWC 1080
HD 1404	00 18 19.657	+36 47 06.81	43	A2V	4.5	4.5	AS 442, MWC 1080

References. (1) Muzerolle et al. 2003; (2) White & Ghez 2001; (3) Eisner et al. 2004; (4) Monnier et al. 2006; (5) Eisner et al. 2005. Calibrator star distances are based on *Hipparcos* parallax measurements (Perryman et al. 1997).

et al. 2005a, 2005b). All targets except one have been previously spatially resolved in the near-IR. HD 141569, which has not been resolved, is thought to possess a disk with a cleared inner region; however, we include the source here to investigate whether any spectral features are spatially resolved even though the continuum emission is not.

Our sample includes four T Tauri stars, pre-main-sequence analogs of solar-type stars like our own sun, and 11 Herbig Ae/Be stars, 2–10 $M_\odot$ pre-main-sequence stars. The main selection criterion in choosing this sample is source brightness (and because Herbig Ae/Be stars are typically brighter than T Tauri stars, our sample has more of the former). Our experimental setup imposes limiting magnitudes of $K \sim 7$ at near-IR wavelengths and $V \sim 12$ at optical wavelengths. We also require that sources be at zenith angles of less than ∼50°, which excludes from our sample any sources with $\delta \lesssim -35°$. Our sample includes most of the sources in the Herbig–Bell catalog (Herbig & Bell 1988), as well as several additional young stars discovered elsewhere, that meet our selection criteria.

2.2. Observations

We obtained KI observations of our sample on UT 2006 November 12 and UT 2007 July 3. KI is a fringe-tracking long baseline near-IR Michelson interferometer combining light from the two 10 m Keck apertures (Colavita & Wizinowich 2003; Colavita et al. 2003). Each of the 10 m apertures is equipped with an adaptive optics (AO) system that corrects phase errors caused by atmospheric turbulence across each telescope pupil, and thereby maintains spatial coherence of the light from the source across each aperture. The AO systems require sources with V magnitudes brighter than ∼12. Optical beam trains transport the light from each aperture through an underground tunnel to delay lines, beam combination optics, and the detector.

The two outputs of the beam combiner are sent into a dewar that contains a HAWAII array. Interferometric fringes are measured by modulating the relative delay of the two input beams and then measuring the modulated intensity level of the combined beams during four "ABCD" detector reads (Colavita 1999). The measured intensities in these reads are also used to measure atmosphere-induced fringe motions, and a servo loop removes these motions to keep the fringe centered near zero phase.

KI normally measures science data in a spatially filtered wide-band channel, with a second output of the beam combiner, dispersed over four channels using a prism, used for group delay tracking. For the observations discussed here, we used a mode where the prism is replaced with a grism providing an order of magnitude higher dispersion, and we used this spectrally dispersed output for our science measurements. The grism, whose properties are described in Eisner et al. (2007b),

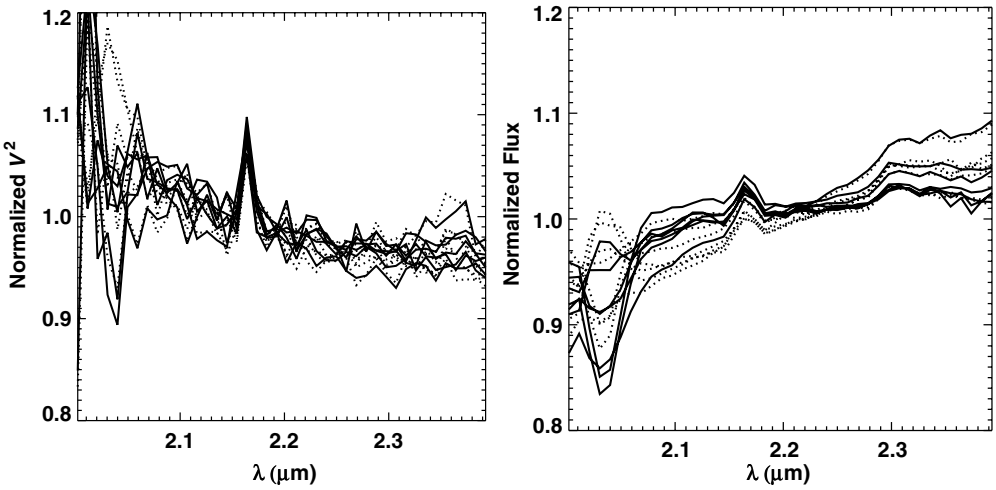

Figure 1. V^2 (left) and fluxes (right) for several scans on the target V1295 Aql. Observations of a calibrator bracketing each target scan were used for calibration, and each line corresponds to one scan. The solid curves show the results when HD 183324 was used as the calibrator, and dotted lines show results when HD 188385 was used. While we average all of these measurements together to determine the average V^2 and fluxes for a target, we plot the results for each scan and calibrator individually here to demonstrate statistical and systematic uncertainties in the data. Note that the strong feature at 2.165 μm appears in all scans, and corresponds to Brγ emission intrinsic to the source.

provides a spectral resolution of $R = 230$, with 42 10 nm wide channels across the K band. To obtain adequate signal-to-noise for the group delay measurement with our grism, which has 10 times more pixels and hence 10 times more read noise than the prism that is normally used, we require a star brighter than $K \sim 7$.

In the following sections, we discuss the calibration, modeling, and interpretation of our V^2 and flux data. We exclude HD 141569 and VV Ser from most of this discussion. HD 141569 is unresolved across our observing band, and thus we can only say that the source is small compared to the fringe spacing at all observed wavelengths. Conversely, we were unable to measure fringes for VV Ser (despite measuring strong K-band flux), and for this object we can only say that the angular size is large compared to the fringe spacing. We defer discussion of these sources to Sections 4.2–4.3.

2.3. V^2 Calibration

We measured squared visibilities (V^2) for our targets and calibrator stars in each of the 42 spectral channels provided by the grism. The calibrator stars are main-sequence stars, with known parallaxes, whose K magnitudes are within 0.5 mags of the target K magnitudes (Table 1). The system visibility (i.e., the point source response of the interferometer) was measured using observations of these calibrators, whose angular sizes were estimated by fitting blackbodies to literature photometry. These size estimates are not crucial since the calibrators are unresolved (i.e., their angular sizes are much smaller than the interferometric fringe spacing) in almost all cases. HD 163955, a calibrator for MWC 275, is mildly resolved; we account for this when computing the system visibility.

We calculated the system visibility appropriate to each target scan by weighting the calibrator data by the internal scatter and the temporal and angular proximity to the target data (Boden et al. 1998). For comparison, we also computed the straight average of the V^2 for all calibrators used for a given source, and the system visibility for the calibrator observations closest in time. These methods all produce results consistent within the measurement uncertainties. We adopt the first method in the analysis that follows.

Source and calibrator data were corrected for standard detection biases as described by Colavita (1999) and averaged into 5 s blocks. We accounted for a known bias related to flux level by applying an empirically determined correction.[6] Calibrated V^2 were then computed by dividing the average measured V^2 over 130 s scans (consisting of 5 s sub-blocks) for targets by the average system visibility. Uncertainties are given by the quadrature addition of the internal scatter in the target data and the uncertainty in the system visibility. We average together all of the calibrated data for a given source to produce a single measurement of V^2 in each spectral channel. The observations of our targets typically spanned $\lesssim$1 hr, and the averaging therefore has a negligible effect on the UV coverage.

We investigate the uncertainties in our calibration procedure in several ways. First, we examine the calibrated V^2 for each scan for one of our targets (V1295 Aql) where we obtained several scans. We also compare calibrated V^2 using one calibrator and another. Differences between scans and between the two calibrators provide an estimate of the uncertainties. Results of this test are shown in Figure 1. Across most of the band, channel-to-channel uncertainties are a few percent or less. However, there is a large dispersion in the various measurements around 2.05 μm.

A second probe of the uncertainties is provided by applying our calibrations to two main-sequence check stars, HD 167564 and HD 171149 (Figure 2). These stars were observed as calibrators for VV Ser, and are 30°–40° away from the other nearest calibrators in our data set. Thus, we expect the uncertainties derived here to be larger than for our target stars, which are within 10° of their calibrators. For these two stars, the standard deviation of the calibrated V^2 across the bandpass is 1%–2%. However, the data for both stars exhibit an apparently systematic feature around 2.05 μm, the same spectral region that exhibits larger uncertainties in Figure 1.

We do not have a simple explanation for these large errors at the short-wavelength end of our band. Telluric CO_2 features lead to absorption (and hence lower photon counts) on either side of 2.05 μm, but not at 2.05 μm; a plot of the atmospheric

[6] http://msc.caltech.edu/software/KISupport/dataMemos/fluxbias.pdf

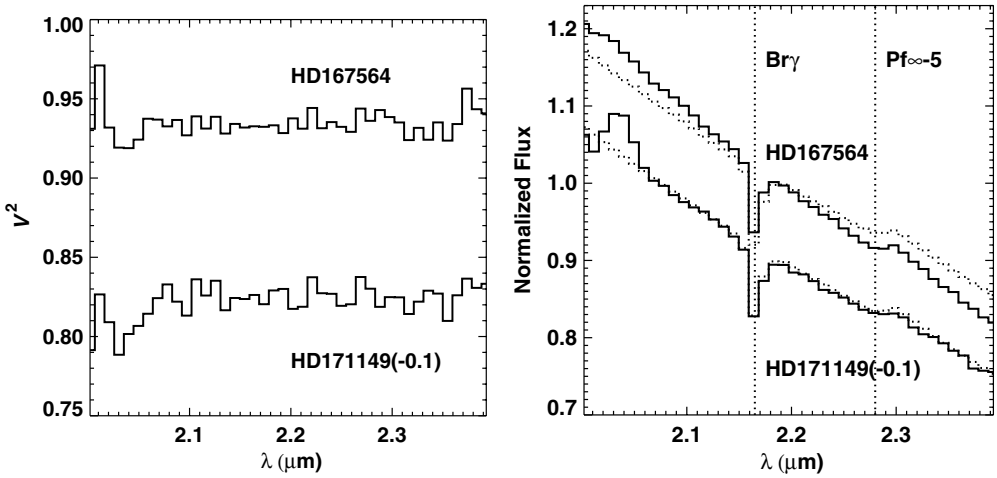

Figure 2. Calibrated V^2 (left) and fluxes (right) for two unresolved check stars. The data for HD 171149 have been shifted down by 0.1 in both plots for ease of presentation. We also plot the fluxes predicted for these stars from Kurucz models (dotted histograms). We applied the same calibrations to these stars as we did to V1295 Aql. However, these stars are $\gtrsim 30^\circ$ away from their calibrator stars, substantially further than any of our targets are from their respective calibrator stars. The calibration uncertainties seen here may therefore be more severe than for any of our target data.

transmission is shown in Figure 3. Furthermore, it is difficult to imagine how any atmospheric or instrumental absorption could vary as quickly as the observed variations and Figure 1 shows that fluxes in this region vary both positively and negatively, contrary to expectations for time-variable absorption. We speculate that the observed variability near 2.05 μm may be due to constructive and destructive interference caused by a known phase irregularity at this wavelength in a dichroic optic.

We adopt 3% channel-to-channel uncertainties for our target stars. However, Figures 1 and 2 indicate that data shortward of $\sim$2.05 μm likely has larger errors, and should be treated with additional caution. The normalization of V^2 versus wavelength (i.e., the average value of V^2 across the band) has an additional uncertainty. Observations of binary stars with known orbits show that the calibrated V^2 have a systematic uncertainty of $\lesssim 3\%$.[7] We therefore assume that in addition to the 3% channel-to-channel uncertainties described above, the normalization of V^2 is uncertain by $\sim 3\%$.

Calibrated V^2 for our sample are shown in Figure 4. As discussed above, HD 141569 and VV Ser are excluded from these plots (and from our subsequent analysis) because they are unresolved and overresolved, respectively, in our observations.

2.4. Flux Calibration

We used the count rates in each channel observed during "foreground integrations" (Colavita 1999) to recover crude spectra for our targets. We divided the measured flux versus wavelength for our targets by the observed fluxes from the calibrator stars, using calibrator scans nearest in time to given target scans, and then multiplied the results by template spectra suitable for the spectral types of the calibrators.

We perform the same tests of our calibration procedure as employed in Section 2.3. Variations in calibrated fluxes for several scans, using different calibrators, suggest that there are uncertainties in the overall slopes of the spectra that lead to channel-to-channel uncertainties of $\sim$ 5%–10% (Figure 1). These slope variations may arise because of different coupling efficiencies of light at different wavelengths into the single-mode fiber feeding the detector; the relative couplings could also change with the atmospheric seeing. Tests of this calibration procedure for main-sequence stars of known spectral type, calibrated using other calibrator stars, indicate channel-to-channel uncertainties of a few percent (Figure 2), and also show evidence for these slope uncertainties.

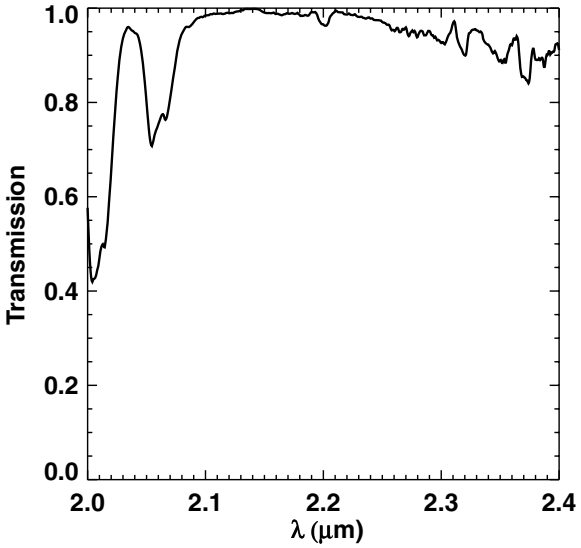

Figure 3. The fractional transmission of the atmosphere over Mauna Kea for 1.6 mm of precipitable water vapor and an airmass of 1.5. The curve has been smoothed to the spectral resolution of our observations. The strong absorptions on either side of 2.05 μm are due to atmospheric CO_2.

Because our measured spectra have these potential slope errors, we use broadband photometry at near-IR wavelengths to infer the correct normalization and slope. We compiled near-IR flux measurements from the literature (Mendoza 1966, 1968; Glass & Penston 1974; Hillenbrand et al. 1992; Kenyon & Hartmann 1995; Skrutskie et al. 1996; Jensen & Mathieu 1997; Malfait et al. 1998; Eiroa et al. 2002; Koresko 2002; Cutri et al. 2003; Prato et al. 2003; Eisner et al. 2004), including multiple measurements where available, and then fitted a straight line to these data. We scaled our measured KI spectra so that the slope and normalization matched those of the fitted lines. With these corrections, the spectra contain information about narrow

[7] http://msc.caltech.edu/software/KISupport/dataMemos/fluxbias.pdf

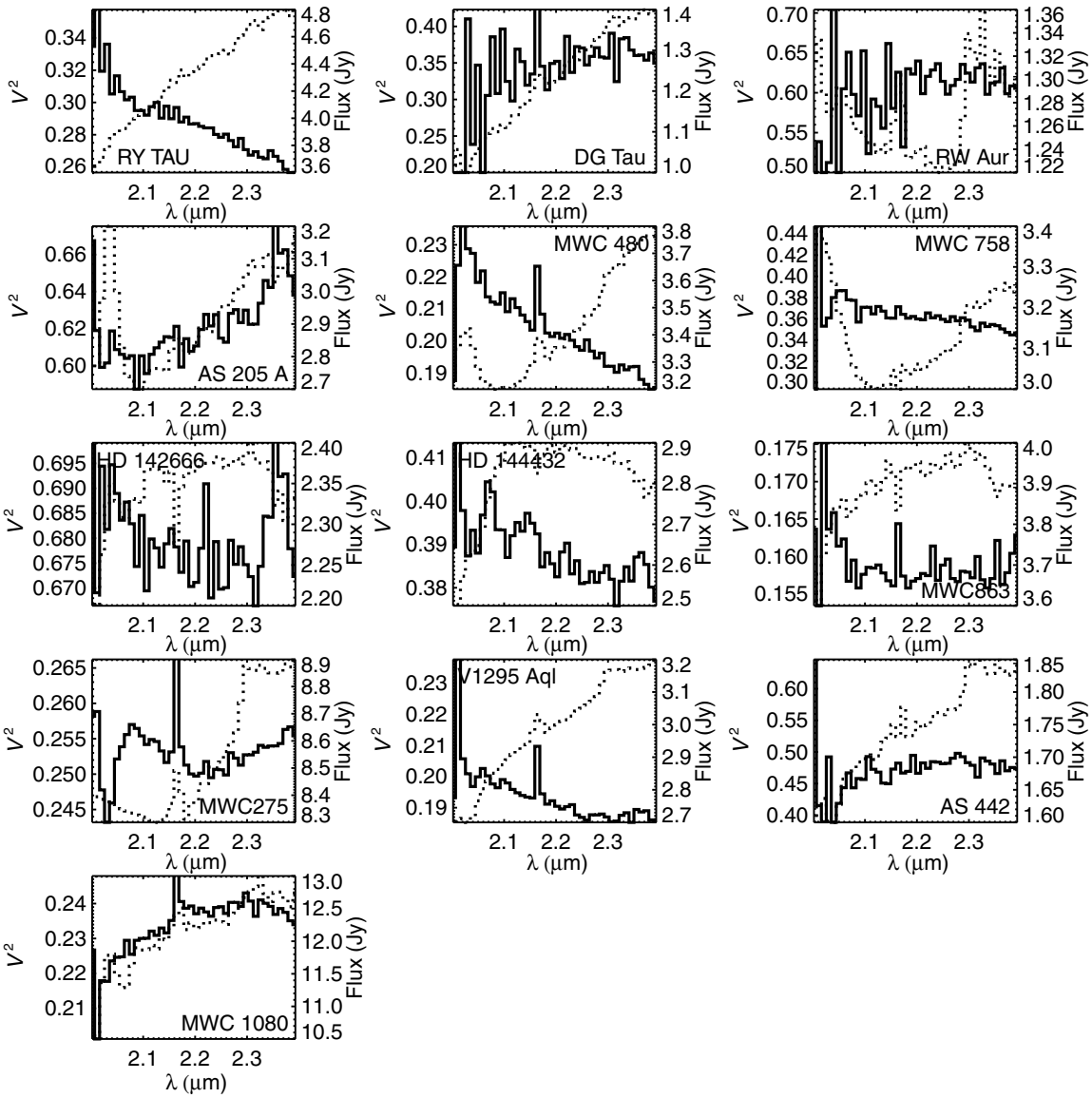

Figure 4. Calibrated V^2 (solid histograms) and fluxes (dotted histograms) for our sample. Channel-to-channel uncertainties are estimated to be 3% for V^2 and 5%–10% for fluxes. For DG Tau and RW Aur, the noise in the measured V^2 is larger for $\lambda \lesssim 2.2$ μm, owing to the low fluxes ($\lesssim 1$ Jy) at these wavelengths.

spectral features, but do not contain any original information about the overall normalization or slope (this information comes from the broadband literature photometry). Moreover, since our targets tend to be photometrically variable, this procedure introduces some additional uncertainty in the absolute flux level at the epoch of our KI observations.

We estimate uncertainties in our calibrated, slope-corrected spectra of 5%–10%. However, Figures 1 and 2 show evidence for larger errors around 2.05 μm. As for the V^2 calibration discussed in Section 2.3, the fluxes in this spectral region should be treated with caution.

2.5. Features of Calibrated V^2 and Fluxes

Figure 4 shows the V^2 and fluxes calibrated with the procedure outlined in Sections 2.3–2.4. The calibrated fluxes typically increase with wavelength across the *K* band, consistent with expectations for warm ($\lesssim$2500 K) circumstellar emission. The V^2 exhibit different behaviors with wavelength, ranging from positive to negative slopes. Interpretation of these V^2 trends requires an accounting of the differing angular resolution of the observations as a function of wavelength, since the resolution gets coarser at longer wavelengths. It is more straightforward to explain the V^2 behavior by first converting the measured V^2 into angular sizes; we do this in Section 3.2.

The fluxes and V^2 do not always behave monotonically across the observing window, due to the presence of spectral features associated with hot hydrogen gas, and warm CO and H_2O vapor. For example, MWC 480, MWC 275, and V1295 Aql show clear bumps in both flux and V^2 near 2.165 μm, associated with the Brγ transition of hydrogen. Spectral features like these may arise in absorption in stellar photospheres, or in emission in the circumstellar material. In Section 3, we determine contributions to the fluxes and V^2 from the central star, enabling investigation of the spectral features arising from the circumstellar emission.

3. MODELING

In this section, we use our V^2 and flux measurements to constrain the distribution of dust and gas within 1 AU of our sample stars. We first consider the simplest possible model for

the emission, a uniform disk (Section 3.2); this model provides an estimate of how the angular size of the emission depends on wavelength, with essentially no model assumptions. We then explore more physically realistic models that include both gas and dust components. Specifically, we model our sources as optically thin gaseous accretion disks that extend as far as the dust sublimation radius, at which point emission from the puffed-up dust sublimation front dominates. We include various gaseous species in the inner disk as needed to fit the data. Because our V^2 and flux measurements contain contributions from both the circumstellar disks and the unresolved central stars of our targets, we remove the stellar component from our measurements before fitting the models described above. The procedure by which stellar and circumstellar components are separated is described in Section 3.1.

3.1. Separating Stellar and Circumstellar Components

Before fitting physical models to the data, we remove the contribution of the central stars from our measurements. This enables us to model only the circumstellar material around our sources. Because the central stars are unresolved, we know that $V_*^2 = 1$, and we need only the ratio of the stellar and circumstellar fluxes to remove the stellar contribution to the measured V^2 and fluxes.

We estimate the circumstellar-to-stellar flux ratio at each observed wavelength using spectral decomposition (see e.g., Millan-Gabet et al. 2001). Using optical photometry from the literature, we fit the stellar photosphere. For each source we assume the spectral type given in the literature (also listed in Table 1) and determine the stellar radius and reddening providing the best fit to the data; the reddening law of Steenman & Thé (1991) is used. In general, we assume that the optical (*VRI*) photometry traces the unveiled stellar photosphere. However, for AS 205 A, we have veiling measurements at *R* and *I* bands from Eisner et al. (2005), and we use these to precisely fit the photospheric flux. We then extrapolate the photosphere to the *K* band using Kurucz models, which include stellar spectral features like Brγ absorption in A stars or CO overtone absorption in cooler stars. We compare the extrapolated stellar fluxes with our measured *K*-band fluxes to determine stellar and circumstellar contributions.

With these circumstellar-to-stellar flux ratios, we remove the stellar components of the visibilities:

$$V^2_{\rm disk} = \left\{ \frac{\sqrt{V^2_{\rm meas}}(1 + F_{\rm disk}/F_*) - 1}{F_{\rm disk}/F_*} \right\}^2, \quad (1)$$

where $F_{\rm disk}/F_*$ is the circumstellar-to-stellar flux ratio. We fit our models for the circumstellar emission to $F_{\rm disk}$ and $V^2_{\rm disk}$ below.

3.2. Uniform Disk Sizes

Before interpreting our data in the context of physical models, we begin with a simple geometrical model: a uniform disk (e.g., Eisner et al. 2003). We fit the $V^2_{\rm disk}$ data for each source, in each channel, with the model. The results, shown in Figure 5, give the "spectral size distribution" of the *K*-band emission, illustrating how the spatial scale of the near-IR emission depends on wavelength.

Figure 5 shows that the angular diameter of the near-IR emission appears to increase with wavelength for all sources in the sample (although the trend is marginal for DG Tau and RW Aur, where the data have lower signal-to-noise). As in previous work (Eisner et al. 2007a; Eisner 2007; Kraus et al. 2008), we interpret this slope as evidence for a hot emission component interior to the inner edge of the dust disk. This hot, compact component increasingly dominates the observed emission at shorter wavelengths, and hence the angular diameter of the emission appears to decrease.

In addition to showing increasing size with wavelength, Figure 5 shows that several objects exhibit emission from the Brγ transition of hydrogen that is more compact than the circumstellar continuum emission. We see indications of compact Brγ emission from MWC 480 (reported previously by Eisner 2007), MWC 758 (marginally), HD 144432 (marginally), MWC 863, MWC 275, V1295 Aql, and MWC 1080.

Finally, we see evidence of angular diameter changes due to CO opacity in RW Aur. Figure 6 shows a zoomed-in view of the spectral region encompassing several CO rovibrational overtone ($\Delta v = 2$) band heads. The flux increases in each of the CO band heads, demonstrating the presence of CO emission in this object. Moreover, the angular diameter appears to decrease within each of the band heads, indicating that the CO emission is more compact than the continuum.

3.3. Accretion Disk Models

As a more physically realistic model, we begin with a dusty circumstellar disk whose emission is dominated by the hottest dust near the sublimation radius, and then include gaseous emission interior to the inner edge of the dust. We consider several different gaseous opacity sources, including continuum emission, Brγ emission, water vapor, and CO. For DG Tau and RW Aur, we do not consider V^2 data measured shortward of 2.1 μm, since low fluxes (<1 Jy) lead to extremely noisy data at these wavelengths (Figure 4).

We do not consider models that include only gaseous emission because previous investigators have shown that ring-like dust sublimation fronts are needed to fit broadband SEDs and interferometry data (e.g., Muzerolle et al. 2003; Eisner et al. 2004). Furthermore, Eisner et al. (2007a) showed that gas-only disk models, while they can potentially reproduce observed spectrally dispersed visibilities, cannot simultaneously reproduce observed SEDs. We therefore do not consider gas-only models here.

We do not fit the broadband SED simultaneously with our 2.0–2.4 μm data set here, to avoid additional complication. Since our modeling is not constrained by SEDs outside of the *K* band, the inferred properties of the circumstellar emission may not perfectly reflect reality. This is especially true for the gaseous emission, which is often more compact than the spatial resolution of our observations. Nevertheless, the modeling presented below demonstrates the presence of gaseous emission components, and provides a rough estimate of the size scales and temperatures of these components.

3.3.1. Dust Continuum Emission

We assume that the dust emission in our model arises from a single-temperature ring of matter at the disk radius where temperatures become hot enough for dust sublimation (as in previous studies; e.g., Eisner et al. 2004). This ring of emission approximates well (Eisner et al. 2004) the puffed-up inner edge expected for directly irradiated inner disks in hydrostatic equilibrium (Dullemond et al. 2001). The width of the ring is assumed to be two tenths of its radius, consistent with calculations of the expected width of the dust sublimation front

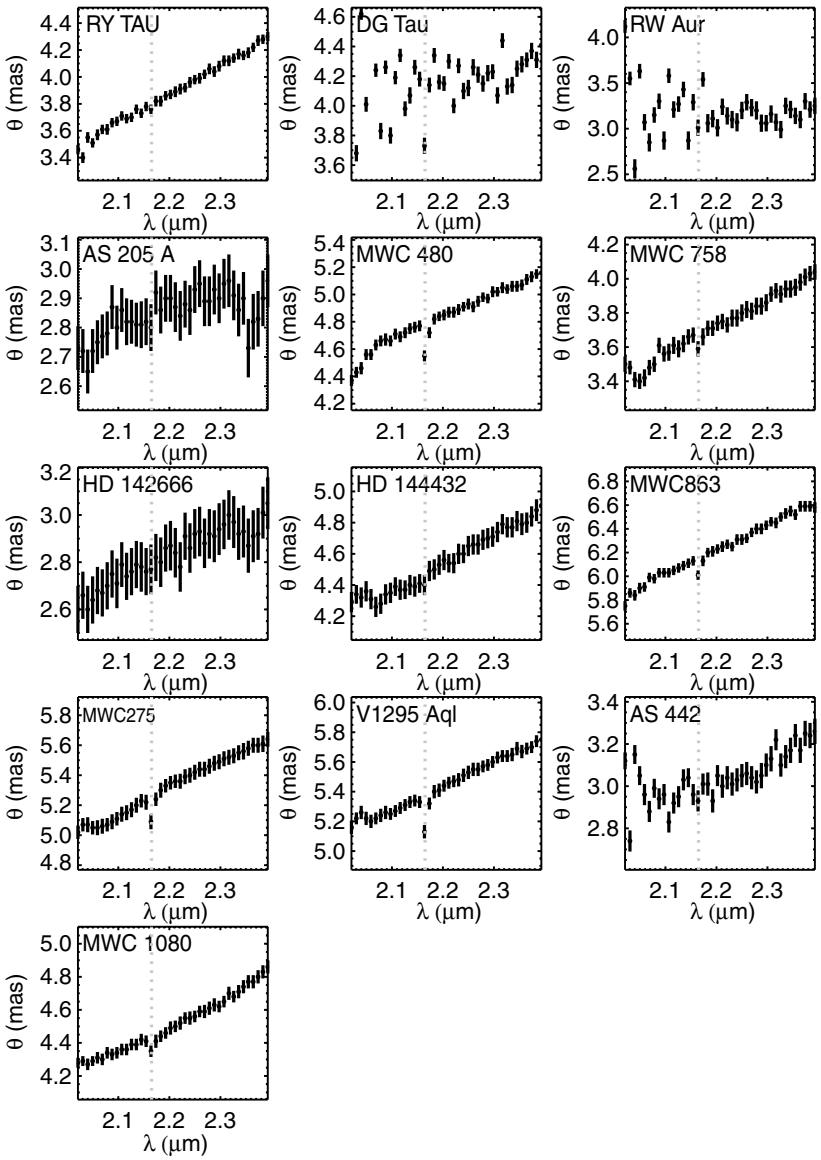

Figure 5. Fitted uniform disk diameter as a function of wavelength for our sample. The dotted line in each panel marks the wavelength of the Brγ transition of hydrogen.

(e.g., Isella & Natta 2005). The free parameters of this model are the radius and temperature of the emission ring, $R_{\rm dust}$ and $T_{\rm dust}$. We determine the best-fit values of these parameters using a grid-based χ^2 minimization. Uncertainties are determined directly from the χ^2 surface (e.g., Eisner et al. 2004).

3.3.2. Gaseous Continuum Emission

We assume that the radial temperature and surface density profiles of the gas in the inner disk are described by power laws. We take $T(R) \propto R^{-1/2}$, as appropriate for optically thin disk material (e.g., Chiang & Goldreich 1997); $T(R)$ is the radial temperature profile and R is the stellocentric radius. Details of the gaseous emission mechanism may alter this relationship, but we will consider the radial temperature law fixed for simplicity. We assume that the surface density is described by $\Sigma(R) \propto R^{-3/2}$, as inferred for the protosolar nebula (Weidenschilling 1977) and assumed in other disk models (e.g., Chiang & Goldreich 1997; Dullemond et al. 2001). The optical depth, τ, is directly related to the surface density, and hence $\tau_\nu(R) \propto R^{-3/2}$. Depending on the normalization of the optical depth profile, the gas may be entirely optically thin, entirely optically thick, or thick in the innermost regions only.

We define the radial temperature and optical depth profiles over an inner disk radius, $R_{\rm in}$, to an outer disk radius, $R_{\rm out}$. We take $R_{\rm out}$ to be the radius of the dust ring described in Section 3.3.1. $R_{\rm in}$ is left as a free parameter.

The free parameters of the gaseous disk model are the inner radius, $R_{\rm in}$, the temperature at the inner radius, $T_{\rm in}$, and the optical depth at the inner radius, $\tau_{\rm in}$. When combined with the dust component, the dust + gas continuum emission model has five free parameters. We determine the values of these parameters that provide the best fit to the data using a Marquardt–Levenberg algorithm. Uncertainties on best-fit parameters are computed from the covariance matrix.

If the gas is optically thick, then only the radial temperature profile is important in determining the resultant flux. However for most sources, simple disk models with optically thick gas predict fluxes larger by an order of magnitude than those observed from our sample. We therefore expect the gas to be (at least partially) optically thin in our modeling. The 2 μm emission from optically thin gaseous disk models arises

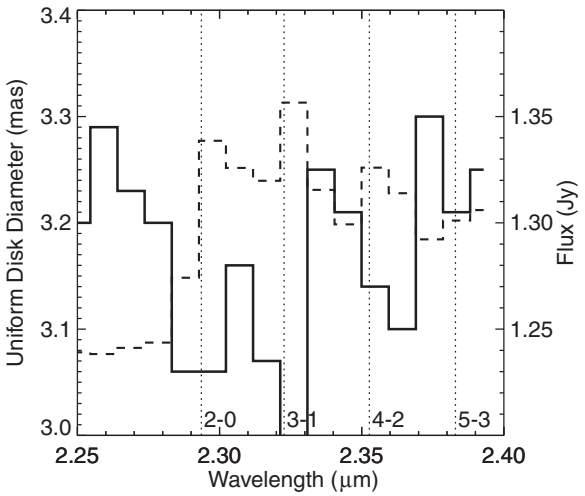

Figure 6. Uniform disk diameter as a function of wavelength for RW Aur A (solid histogram) in the spectral region of the CO overtone band heads. The measured fluxes in this region are also plotted (dashed histogram). Dotted lines show the wavelengths of the CO overtone band heads. The uncertainties on measured sizes and fluxes, which can be found in Figures 5 and 7, are ∼5%.

predominantly from the innermost radii. Models including dust and optically thin gas thus resemble two-ring models (like those considered in Eisner et al. 2007a), where hot gaseous emission appears in a ring near the inner radius and warm dust emission arises from the ring-like dust sublimation front.

3.3.3. Water Vapor Emission

Several objects in our sample show additional flux, and accompanying broad features in V^2, at wavelengths $\lesssim 2.1$ μm. These features are (in some cases) broader than the systematic features discussed in Section 2.2, although the data are still affected by these short-wavelength systematic effects. In a previous paper, we reported such features for MWC 480, and modeled the data by adding a single-temperature ring with the opacity of water vapor to a two-ring dust + gas model (Eisner 2007). Here we refine this simple model, and test whether the data for our sources can be fitted with a model where water vapor emission occurs over a range of radii from an inner radius where water is thermally dissociated out to the dust sublimation radius.

We use opacities measured for water vapor (Ludwig 1971) at a range of temperatures ($\sim$ 1000–3000 K) appropriate to protoplanetary disks. Using the gaseous disk model described in Section 3.3.2, we determine the optical depth at each radius using the assumed surface density profile, which scales as $\Sigma(R) \propto R^{-3/2}$: $\tau_\nu(R) = \Sigma(R)\kappa_\nu$. For disk radii where $T < 3000$ K, water vapor can exist and we use κ_ν from Ludwig (1971). At smaller stellocentric radii, where water would be dissociated, we retain the assumption of continuum emission. While it is also possible that water emission, where is exists, adds to rather than replaces the underlying continuum, we do not consider this possibility in our simple model.

3.3.4. Brackett Gamma Emission

Figures 4 and 5 show that Brγ emission signatures are present in the flux and V^2 data for several objects. In fact, flat spectra in the vicinity of the Brγ wavelength (2.165 μm) may indicate the presence of Brγ emission for some objects. Since more massive stars, including essentially all of the Herbig Ae/Be stars in our sample, have photospheric Brγ absorption, nondetection of this absorption feature in the spectra implies that circumstellar Brγ emission (and continuum excess) is filling in the feature. The effects of photospheric Brγ absorption are included in the Kurucz models we used to separate stellar and circumstellar components of the measured V^2 and fluxes (Section 3.1).

We model circumstellar Brγ emission by including additional flux in the gaseous component of our models at 2.165 μm. Since Brγ traces very hot gas ($\sim 10^4$ K), we assume that the emission arises from the innermost disk annulus. In fact, Brγ emission may be even more compact, but we cannot constrain such small size scales with the available angular resolution. Inclusion of Brγ emission in the model introduces as an additional free parameter the gaseous line-to-continuum ratio in the innermost gaseous annulus.

4. RESULTS

4.1. Dust and Gas within 1 AU of Young Stars

Our modeling clearly shows that single-temperature rings of emission cannot fit the data for our sample (Figure 7; Table 2). This confirms previous inferences from spectrally dispersed interferometric results (Eisner et al. 2007a; Eisner 2007; Kraus et al. 2008; Isella et al. 2008) and from high angular resolution continuum observations (Tannirkulam et al. 2008). The implication is that models where all of the near-IR emission arises from the inner edge of the dusty disk are untenable. Rather, a warm dusty component and a hotter, presumably gaseous, component at smaller stellocentric radii are required to fit the data.

The simple dust + gas continuum model (Section 3.3) predicts V^2 and fluxes compatible with the observations for most sources (Figure 7). We also consider a model where the gaseous opacity is due to water vapor at stellocentric radii where H_2O can potentially exist. As shown in Figure 7, these models generally produce fits of comparable quality to the simple continuum models. Models including water vapor also produce more physically realistic fitted values of $R_{\rm dust}$: the fitted dust temperatures are between $\sim$ 1200 and 1500 K, in agreement with expected sublimation temperatures for silicate dust in protoplanetary disks (e.g., Pollack et al. 1994). However, for RY Tau, the simple dust + gas (continuum) model produces a superior fit to the data.

We illustrate the relative contributions of gas and dust to our models in Figure 8. The figure shows the fluxes produced by the gaseous component and the dust component for our best-fit models including water vapor opacity. The gaseous component includes continuum emission, water vapor emission, and Brγ emission. In all cases, the gaseous flux represents a significant fraction of the total.

For all sources except AS 205 A, the best-fit dust + water model requires emission from material substantially hotter than 3000 K (Table 2), implying the presence of substantial gaseous continuum emission. The inferred inner disk temperatures for models including water vapor opacity are, in most cases, higher than for models assuming only gas continuum opacity. This difference suggests that the best fit for models including water vapor requires the gaseous emission to be dominated by the hot continuum component rather than the cooler water vapor component. For AS 205 A, in contrast, it appears that water vapor alone can explain the observed gaseous emission from the inner disk.

RW Aur shows evidence of spatially resolved CO in the inner disk. Emission from the $\Delta v = 2$–0, 3–1, and 4–2 band heads is

Table 2
Results of Modeling

Source	χ_r^2	T_{in} (K)	R_{in} (AU)	τ_{in}	T_{dust} (K)	R_{dust} (AU)
			Dust Models			
RY Tau	44.34				1750 ± 10	0.16 ± 0.01
MWC 480	31.85				1450 ± 10	0.20 ± 0.01
MWC 758	17.89				1610 ± 10	0.17 ± 0.01
DG Tau	4.70				1260 ± 10	0.18 ± 0.01
RW Aur	3.60				1330 ± 10	0.14 ± 0.01
HD 142666	1.55				1670 ± 10	0.10 ± 0.01
HD 144432	10.92				1420 ± 10	0.20 ± 0.01
MWC 863A	41.40				1360 ± 10	0.28 ± 0.01
V1295 Aql	25.20				1350 ± 10	0.48 ± 0.01
AS 205A	2.08				1850 ± 10	0.14 ± 0.01
MWC 275	19.93				1750 ± 10	0.20 ± 0.01
AS 442	8.63				1580 ± 10	0.57 ± 0.01
MWC 1080	24.39				2190 ± 10	1.39 ± 0.01
			Dust + Gas Continuum Models			
RY Tau	0.30	2684 ± 371	0.02 ± 0.04	1.623 ± 4.655	1105 ± 110	0.31 ± 0.02
MWC 480	1.04	3199 ± 391	0.07 ± 0.01	0.081 ± 0.029	1105 ± 9	0.28 ± 0.01
MWC 758	1.73	3462 ± 167	0.07 ± 0.01	0.104 ± 0.013	849 ± 53	0.35 ± 0.03
DG Tau	1.48	2188 ± 423	0.01 ± 0.01	2.000 ± 0.001	1137 ± 29	0.21 ± 0.01
RW Aur	1.71	7125 ± 981	0.02 ± 0.01	0.009 ± 0.001	1233 ± 26	0.15 ± 0.01
HD 142666	0.13	5577 ± 22197	0.01 ± 0.12	0.175 ± 0.989	1236 ± 736	0.14 ± 0.07
HD 144432	0.54	3910 ± 479	0.07 ± 0.01	0.048 ± 0.015	1031 ± 19	0.29 ± 0.01
MWC 863A	0.67	7714 ± 88	0.07 ± 0.01	0.009 ± 0.001	1128 ± 5	0.35 ± 0.01
V1295 Aql	0.58	3115 ± 464	0.14 ± 0.01	0.063 ± 0.029	1106 ± 10	0.62 ± 0.01
AS 205A	0.58	6952 ± 3684	0.01 ± 0.01	2.000 ± 0.001	1461 ± 68	0.18 ± 0.01
MWC 275	0.13	3983 ± 544	0.06 ± 0.01	0.129 ± 0.045	1230 ± 14	0.28 ± 0.01
AS 442	2.70	2521 ± 924	0.29 ± 0.04	0.199 ± 0.282	681 ± 1688	1.34 ± 4.36
MWC 1080	0.67	2790 ± 218	0.50 ± 0.01	0.687 ± 0.173	1271 ± 14	2.33 ± 0.04
			Dust + Water Models			
RY Tau	2.21	5427 ± 654	0.02 ± 0.01	0.238 ± 0.055	1211 ± 4	0.26 ± 0.09
MWC 480	2.46	4659 ± 799	0.02 ± 0.01	0.173 ± 0.084	1246 ± 3	0.25 ± 0.10
MWC 758	2.41	4632 ± 738	0.02 ± 0.01	0.201 ± 0.064	1241 ± 4	0.24 ± 0.08
DG Tau	1.56	16907 ± 470	0.01 ± 0.06	0.020 ± 0.273	1204 ± 18	0.19 ± 0.09
RW Aur	1.68	6114 ± 2414	0.03 ± 0.01	0.009 ± 0.000	1226 ± 25	0.15 ± 0.01
HD 142666	0.25	7334 ± 6398	0.01 ± 0.01	0.757 ± 1.496	1396 ± 5	0.12 ± 0.28
HD 144432	1.13	6812 ± 3310	0.01 ± 0.01	0.574 ± 0.711	1225 ± 2	0.25 ± 0.24
MWC 863A	2.55	5090 ± 1149	0.01 ± 0.01	0.187 ± 0.103	1218 ± 2	0.33 ± 0.14
V1295 Aql	1.68	5368 ± 1560	0.02 ± 0.01	0.232 ± 0.053	1222 ± 1	0.55 ± 0.32
AS 205A	0.48	4222 ± 2727	0.01 ± 0.01	0.611 ± 0.602	1631 ± 6	0.16 ± 0.14
MWC 275	0.57	5271 ± 897	0.02 ± 0.01	0.246 ± 0.059	1409 ± 4	0.25 ± 0.19
AS 442	2.92	13212 ± 14239	0.01 ± 0.01	2.093 ± 7.427	1375 ± 3	0.67 ± 2.54
MWC 1080	1.39	10730 ± 2952	0.06 ± 0.04	0.782 ± 0.750	1600 ± 9	1.90 ± 3.33

detected in our spectra, and appears to be more compact than the surrounding continuum emission (Figure 6). This suggests an origin of the CO interior to the dust sublimation radius. The inferred size of the CO emission for this object is compatible with that inferred from modeling of a high-dispersion spectrum in terms of a Keplerian disk model (Najita et al. 2003).

DG Tau, which is also known to possess CO overtone emission (e.g., Carr 1989), shows no evidence of such emission in our data. This discrepancy may be due to the poor quality of our data for this object or to variability. The CO emission from DG Tau is known to be variable from studies at multiple epochs (e.g., Carr 1989; Najita et al. 2000, 2003), and some previous studies failed to detect the emission (e.g., Greene & Lada 1996).

MWC 758, MWC 275, V1295 Aql, and AS 442 all show excess flux longward of ∼2.3 μm, consistent with the presence of CO overtone emission (Figure 4). However, none of these show evidence in the visibilities of size differences between CO emission and continuum. Given the signal-to-noise and spectral resolution of our current data, we do not attempt to model the CO emission from any of these targets here.

Several objects exhibit Brγ emission from hot hydrogen gas, and this emission is more compact than the surrounding continuum emission in all cases. Table 3 lists the inferred stellocentric radii from which the Brγ emission originates. However, we have somewhat arbitrarily placed the Brγ emission at the innermost edge of the gaseous accretion disk in our models (Section 3.3.4). Since the angular resolution of our observations is ∼0.1 AU, and there is some degeneracy in our models between the Brγ flux and angular scale, we can only state confidently that the Brγ emission arises from radii less than 0.1 AU.

While our model fits indicate that Brγ emission is present around RW Aur, and is more compact than the continuum,

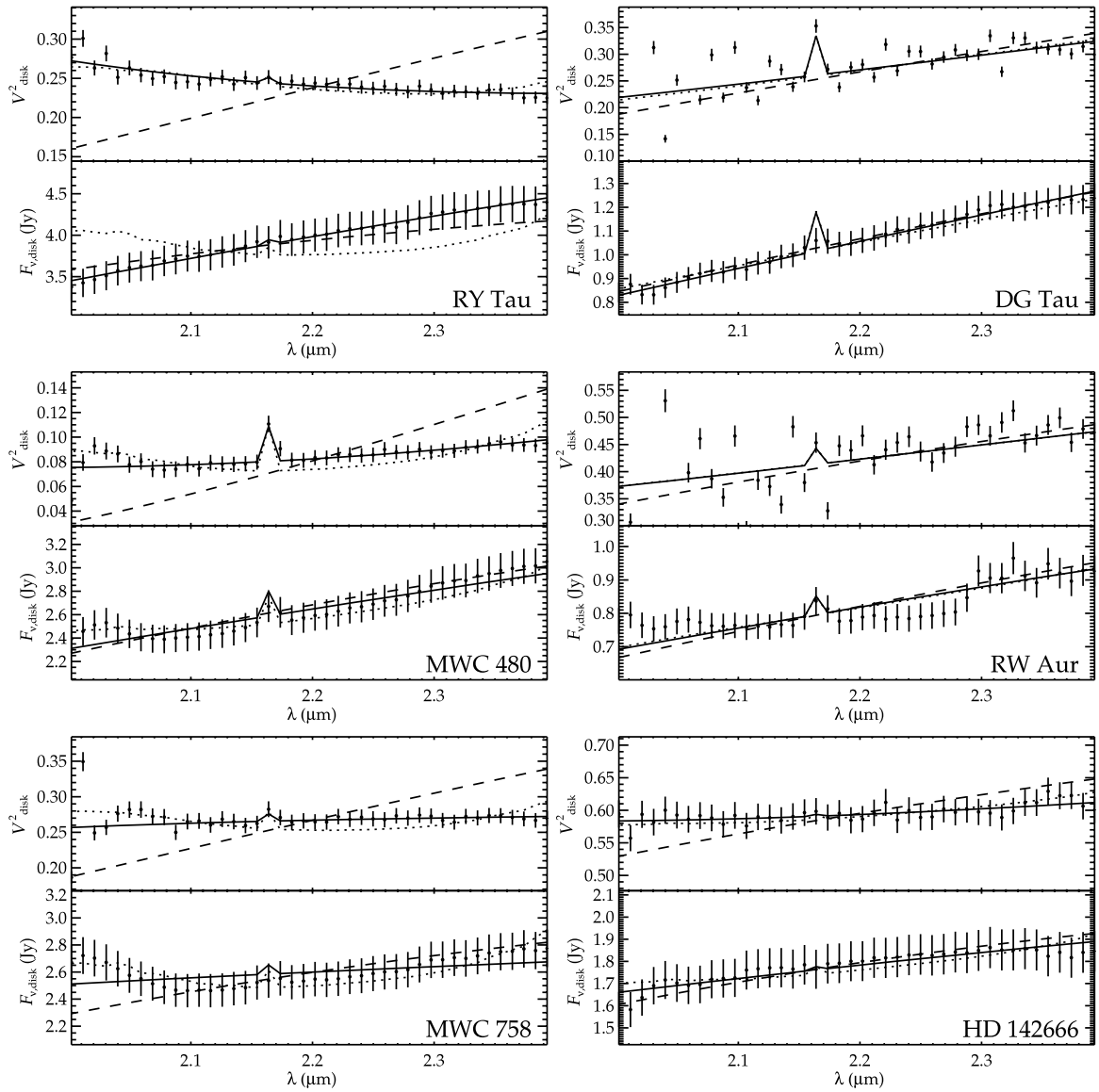

Figure 7. Circumstellar components of measured V^2 and fluxes for our sample, as a function of wavelength, with the predictions of various models. Dashed curves show the predictions of models including a single-temperature ring of (dust) emission. Solid curves represent a model that includes a gaseous inner disk that emits continuum emission and Brγ emission, in addition to the dust ring. Dotted curves show the predictions of models that include the effects of water vapor opacity in the gaseous emission.

we are not confident in this result given the large uncertainties on V^2 for this source in this spectral region. The data for DG Tau also show evidence for compact Brγ emission, but the noisy data in this spectral region argue for a cautious interpretation. Both DG Tau and RW Aur have previously detected (spatially unresolved) Brγ emission (Folha & Emerson 2001; Najita et al. 1996b), providing some support for our tentative detections.

MWC 480, HD 144432, MWC 863, V1295 Aql, and MWC 275, all targets that exhibit compact Brγ emission, were previously reported to show strong Brγ emission in high-dispersion (spatially unresolved) spectroscopic observations (Garcia Lopez et al. 2006; Brittain et al. 2007; Berthoud 2008). RY Tau, MWC 758, HD 142666, and AS 205 also have previously reported Brγ emission (Najita et al. 1996b; Folha & Emerson 2001; Garcia Lopez et al. 2006; Berthoud 2008). However, the equivalent widths of the Brγ emission are small relative to other sources (e.g., MWC 275 or DG Tau), and it is not surprising that we do not detect (or only marginally detect) Brγ emission from these objects here.

4.2. An Unresolved Source: HD 141569

Previous near-IR interferometric observations of HD 141569 found it to be unresolved in the K band, suggesting that the K-band emission is produced entirely by the unresolved central star. We reobserved it here to search for spatially extended circumstellar emission associated with gaseous spectral features, which might have been washed out in the previous, broadband observations. The observations presented here, however, show that the source is unresolved at all wavelengths. We also see no evidence of flux above the level expected from the stellar photosphere at any observed wavelength. We conclude that the emission in each of the spectral channels included in our observations is more compact than ∼0.1 AU (at the target distance), as expected for stellar emission. We may also infer that no

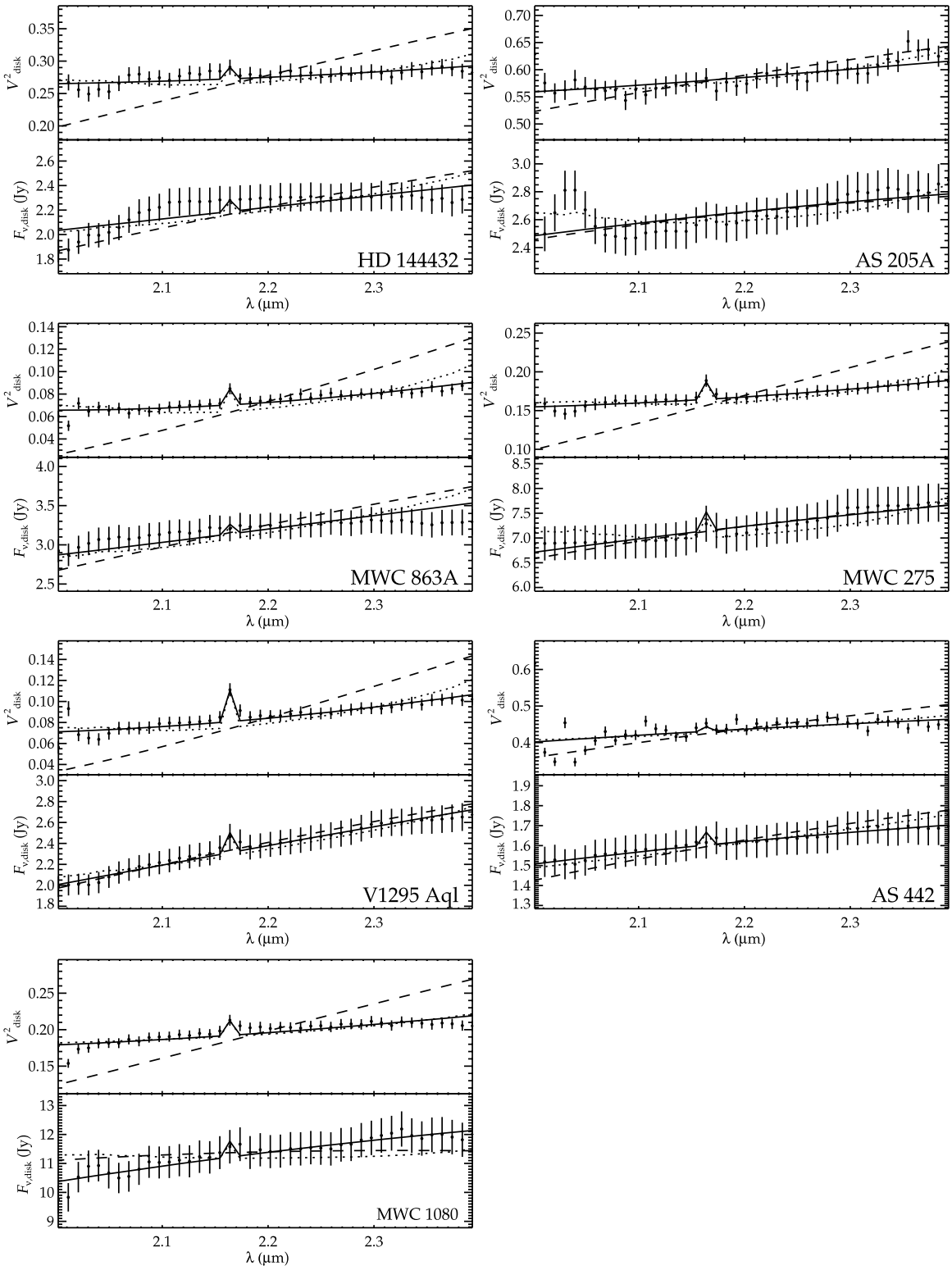

Figure 7. (Continued)

spectral channels contain emission brighter than ∼1% of the stellar flux within the 50 mas field of view of KI (corresponding to stellocentric radii of ∼2.5 AU for this target), since the incoherent contribution of any stronger extended emission would have reduced the measured visibilities. Our finding is consistent with previous studies that found gaseous emission only at stellocentric radii $\gtrsim$ 10 AU (Goto et al. 2006; Brittain et al. 2007), with no warm gas that could have been detected in our observations.

4.3. An Over-resolved Source: VV Ser

One of the objects in our sample, VV Ser, appears to be overresolved in our observations. That is, while we detect flux

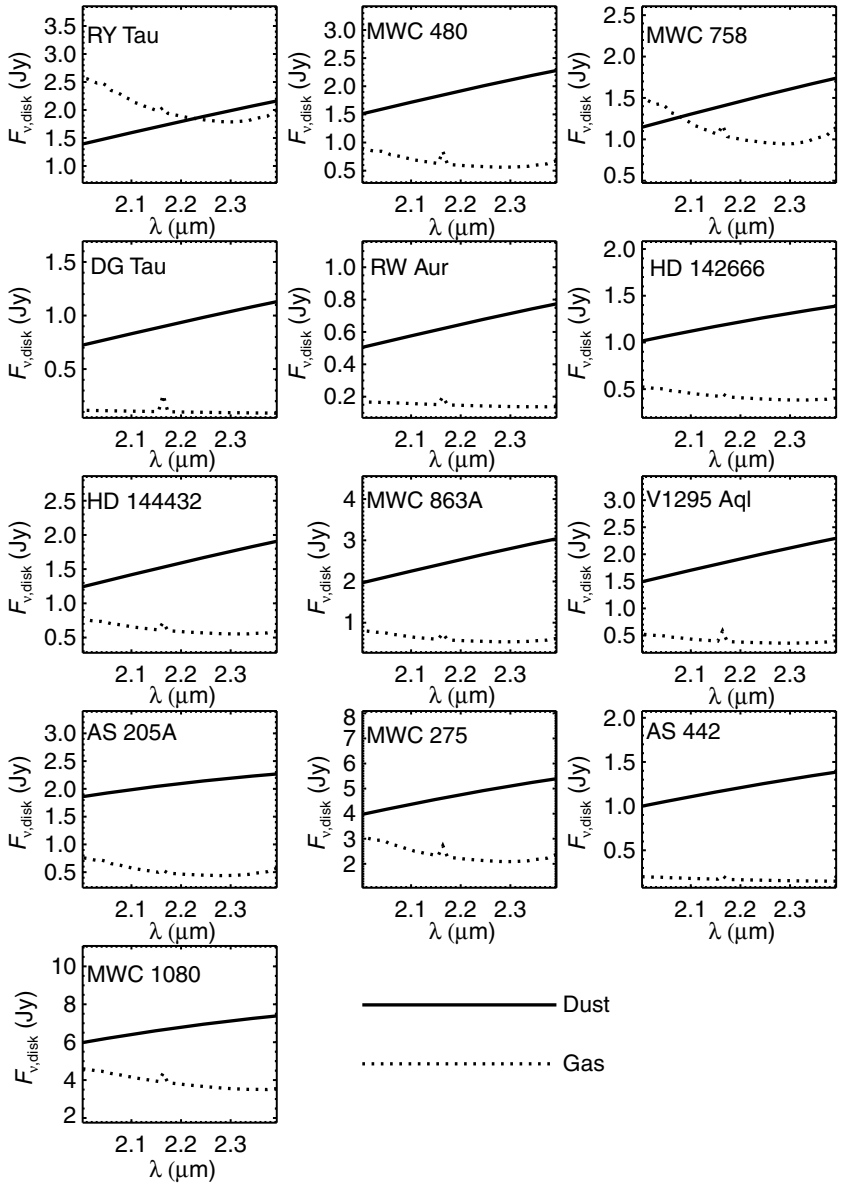

Figure 8. Spectra of best-fit dust + water models, decomposed into dust (solid curves) and gas components (dotted curves). The parameters of the models are given in Table 2. The gaseous component includes continuum emission from material hotter than 3000 K, water vapor emission from gas cooler than 3000 K, and Brγ emission.

from the object, its angular size is large compared to the ∼5 mas fringe spacing and hence its V^2 is undetectably close to zero. Because we can only place a lower limit on the size of the emission, and cannot trace how the size depends on wavelength, we have excluded VV Ser from the analysis presented above.

Previous observations of VV Ser, with fringe spacings comparable to those obtained in the present study, measured a uniform disk angular diameter of ∼4 mas, and showed the disk to be nearly edge-on (Eisner et al. 2003, 2004). Our present nondetection indicates that the size scale of the *K*-band emission has varied significantly between 2003 and 2007. The source is also known to be photometrically variable at optical through infrared wavelengths (e.g., Herbst & Shevchenko 1999; Eiroa et al. 2002).

These findings may indicate variability associated with the UX Ori phenomenon. In this scenario, a vertically extended inner edge of the nearly edge-on disk around VV Ser periodically blocks the central star (e.g., Dullemond et al. 2003; Pontoppidan et al. 2007). When the star is blocked, the near-IR emission would be dominated by the extended circumstellar component, whereas when the star is visible, the observed size would be the flux-weighted average of the unresolved star and the disk.

5. DISCUSSION

5.1. Compact Brγ Emission

We observe Brγ emission from several of our targets, and in all cases this line emission appears more compact than the surrounding continuum. This contrasts with previous results that found Brγ emission more extended than (Malbet et al. 2007) or on a comparable spatial scale to (Tatulli et al. 2007) the dust continuum. Sources where Brγ appears more extended are high-mass stars, and Eisner (2007) speculated that the Brγ emission from young stars may trace both infalling and

Table 3
Properties of Brγ Emission

Source	Dust + Gas Model		Dust + Water Model	
	$R_{\mathrm{Br}\gamma}$ (AU)	$F_{\mathrm{Br}\gamma}/F_{\mathrm{cont}}$	$R_{\mathrm{Br}\gamma}$ (AU)	$F_{\mathrm{Br}\gamma}/F_{\mathrm{cont}}$
RY Tau	0.02 ± 0.04	0.01 ± 0.03	0.07 ± 0.01	0.02 ± 0.02
MWC 480	0.07 ± 0.01	0.08 ± 0.02	0.01 ± 0.01	0.09 ± 0.03
MWC 758	0.02 ± 0.01	0.03 ± 0.03	0.01 ± 0.16	0.05 ± 0.02
DG Tau	0.07 ± 0.01	0.16 ± 0.04	0.07 ± 0.01	0.16 ± 1.13
RW Aur	0.07 ± 0.01	0.06 ± 0.04	0.01 ± 0.01	0.06 ± 0.05
HD 142666	0.05 ± 0.01	0.01 ± 0.05	0.05 ± 0.01	0.02 ± 0.05
HD 144432	0.07 ± 0.01	0.04 ± 0.03	0.02 ± 0.01	0.05 ± 0.05
MWC 863A	0.02 ± 0.01	0.04 ± 0.01	0.02 ± 0.01	0.05 ± 0.02
V1295 Aql	0.01 ± 0.12	0.08 ± 0.02	0.06 ± 0.02	0.09 ± 0.02
AS 205A	0.01 ± 0.01	0.01 ± 0.01	0.01 ± 0.01	0.02 ± 0.04
MWC 275	0.01 ± 0.01	0.05 ± 0.02	0.01 ± 0.01	0.06 ± 0.02
AS 442	0.05 ± 0.05	0.04 ± 0.19	0.12 ± 0.03	0.03 ± 0.06
MWC 1080	0.01 ± 0.02	0.05 ± 0.02	0.06 ± 0.04	0.04 ± 0.02

Notes. The uncertainties listed here are 1σ statistical errors for our model fits. As discussed in Section 4.1, these error bars are probably too small for $R_{\mathrm{Br}\gamma}$, although we can state confidently that $R_{\mathrm{Br}\gamma} < 0.1$ AU for these sources.

outflowing components, with the latter increasingly dominant for higher mass stars.

The results presented here belie this hypothesis. We observe Brγ emission to be more compact than dust continuum in sources spanning a range of spectral types, from K3 to B0. Based on our current findings, we suggest that young stars typically produce most of their Brγ emission close to their central stars in accretion columns and/or shocks. Brγ emission in extended winds seems rarely to be strong enough to dominate the line emission. However, given the small number of Herbig Be stars observed to date, the picture is less clear for higher mass ($\gtrsim 10\ M_{\odot}$) stars.

5.2. Inner Disk Gas: Trends with Stellar Luminosity

For the majority of our sources, models that include only dust emission do not fit the data well, while models including hot gaseous emission interior to the dust sublimation do fit the data (Section 4.1). However, if we examine only the less luminous stars in our sample, the T Tauri stars, we find that this conclusion is less robust. For all of the T Tauri stars in our sample (RY Tau, DG Tau, RW Aur, and AS 205), dust-only models can provide relatively good matches to the slopes seen for fluxes and V^2. Models including gas and dust are still superior, but the difference is not nearly as pronounced as for the more massive Herbig Ae/Be stars in our sample.

We suggest a simple explanation for this trend. For T Tauri sources, the less luminous central stars provide less heating and hence the dust can exist closer to the star than for the more massive Herbig stars. While gaseous disks are likely to extend in to similar radii in both types of sources, the gas may be hotter near to more luminous stars. Higher mass stars have a larger temperature difference between hot gas and warm dust, and also a larger spatial separation of the two components, producing larger temperature gradients. These larger gradients, in turn, lead to larger slopes in the V^2 and fluxes versus wavelength.

This is not to say that T Tauri stars do not have significant gaseous emission. Models including gaseous emission provide superior fits to our data, and previous authors have argued that gaseous emission is needed to self-consistently model SEDs and visibilities (Akeson et al. 2005b). Furthermore, modeling of observed gaseous emission line profiles from T Tauri stars under the assumption of Keplerian rotation has provided evidence for gaseous emission interior to the dust sublimation radius (e.g., Najita et al. 2007). However, the observed temperature gradients between dust and gas appear less pronounced than do those around higher mass stars.

5.3. The Nature of the Gaseous Opacity

Water is predicted to be abundant in the inner regions of disks (e.g., Gorti & Hollenbach 2004), although it can be reduced in abundance in highly irradiated disks (e.g., Thi & Bik 2005). Muzerolle et al. (2004) predict that dust-free inner disks will commonly show water in emission or absorption depending on the disk accretion rate (see also Calvet et al. 1991). However, near-IR water spectral features are detected only rarely in T Tauri stars (e.g., Carr et al. 2004; Najita et al. 2007) and have only been reported in a few Herbig Ae/Be stars (Thi & Bik 2005, Najita et al. 2009).

For most sources, a model that includes water vapor can fit the data well. For AS 205 A, it appears that water vapor alone can reproduce the observed gaseous emission interior to the dust sublimation radius. This is consistent with the detection of abundant water vapor, and an inferred origin at stellocentric radii as small as 0.3 AU, in high-dispersion *L*-band spectra of AS 205 (Salyk et al. 2008).

However, in some cases (e.g., for RY Tau), models including water vapor provide fits of lesser quality than models where the gas emits only continuum radiation. Furthermore, for all sources except AS 205 A, our best-fit models require continuum emission in addition to water vapor emission, since the gas is inferred to be hotter than 3000 K in the innermost regions. This casts some doubt as to whether H_2O emission is needed to fit the data in all cases.

For the columns of water vapor implied by our best-fit models, one might expect our targets to show H_2O emission lines in lower spatial resolution spectroscopic data. High-dispersion spectroscopic observations of several of our sample objects in the *K* band failed to detect strong water emission lines (Najita et al. 2009; Mandell et al. 2008), and archival *Infrared Space Observatory* (*ISO*) data from the Short Wavelength Spectrometer (SWS) for many of our targets do not show longer wavelength H_2O features that typically accompany the 2 μm features modeled in this work. These null results provide further reason to question whether water vapor is a viable explanation for the observed compact, hot, circumstellar continuum emission from some of our sample.

We therefore pose the question: what can produce gaseous continuum emission in the inner regions of protoplanetary disks? We discuss several possible explanations below, and argue that emission from free–free transitions of hydrogen and from the negative hydrogen ion is the most viable mechanism.

5.3.1. Refractory Dust Grains

While dust grains produce continuum emission, the inferred temperatures of the hot component (>3000 K) in our data are higher than the sublimation temperatures for even the most refractory dust grains (e.g., Pollack et al. 1994). Even for calcium-, magnesium-, or titanium-rich oxides, sublimation temperatures above 2000 K occur only for ambient pressures higher than 0.1–1 bar (e.g., Lewis 1997), orders of magnitude larger than the pressures expected in protoplanetary disks (< 0.01 bar for typical densities and temperatures in inner disk regions; e.g., Muzerolle et al. 2004). Dust emission therefore

seems highly implausible as an explanation for the hot, compact emission.

5.3.2. *High*-n *Atomic Hydrogen*

Recombination of photoionized hydrogen into high-n states may also produce a (pseudo) continuum opacity. This mechanism is also probably responsible for the Brγ emission observed toward many of our targets, since it produces hydrogen in the $n = 7$ level, which can then cascade down to the $n = 4$ level and produce the line emission. Even higher-n states, which are longer lived, might be able to produce more extended and continuum-like emission. Photoionization cross sections for these high-n states are $\sim 10^{-18}$ cm^{-2}, and so assuming a gas column density of $\sim 10^{27}$ cm^{-2} (a typical value for young stars accreting material at $\sim 10^{-8} M_{\odot}$ yr^{-1}; e.g., Muzerolle et al. 2004), we see that a fractional abundance of these high-n states of $\gtrsim 10^{-9}$ would be needed to produce an optical depth larger than unity. Estimating the fractional abundance requires knowledge of the ionization and radiation structure of the disk, which is beyond the scope of this paper. However, it seems plausible that recombination to high-n hydrogen states could contribute some opacity in the inner disk.

5.3.3. *Free–Free*

Free–free radiation, produced in ionized winds or accretion columns, or in disks (as for classical Be stars), may also produce continuum emission. Free–free emission may occur around the higher mass stars in our sample, which produce more intense ionizing radiation fields, or in shocked, infalling gas around lower mass stars. The cross section of free–free emission at wavelengths around 2 μm is $\sim 10^{-25}$ cm^4 dyne^{-1} at temperatures of a few thousand Kelvin. Assuming the free–free emission arises in a disk with a gas temperature of 3000 K, a gas column density of 10^{27} cm^{-2}, a fractional ionization of 10^{-5}, and $H/H_2 = 0.01$, we find an electron pressure of ~ 0.01 dyne cm^{-2}, and an optical depth of ~ 0.01. Fractional ionizations of 10^{-5} can arise from the ionization of metals with low ionization potentials, such as Na or Fe; higher fractional ionizations are difficult to achieve since photons with > 11 eV are unlikely to penetrate deeply into such a dense disk. However, somewhat higher optical depths of free–free emission may be achieved if the gas column density is higher than the value assumed above. Some of our targets may be accreting faster than $10^{-8} M_{\odot}$ yr^{-1}, leading to higher gas columns and more free–free emission. It thus seems possible that free–free emission could contribute significantly in the inner disk.

5.3.4. *H*$^-$

The negative hydrogen ion, H$^-$, appears as a promising candidate for explaining this emission, since it can produce free–free continuum emission in the K band (e.g., Chandrasekhar & Breen 1946; Bell & Berrington 1987; John 1988; Gray 1992). For free–free emission from H$^-$ at $\sim$3000 K in the K band, the optical depth is (following Gray 1992)

$$\tau \sim 10^{-38} \left(\frac{n_e}{\mathrm{cm}^{-3}}\right) \left(\frac{N_H}{\mathrm{cm}^{-2}}\right). \quad (2)$$

With the same assumptions as in Section 5.3.3, we find an optical depth of $\sim$0.01 in the inner disk. As above, higher gas columns may lead to correspondingly higher optical depths. Free–free emission from H$^-$ therefore seems like a plausible explanation for the hot, compact emission seen in our data.

6. CONCLUSIONS

We presented spatially resolved near-IR spectroscopic observations that probed the gas and dust in the inner disks around 15 young stars. One source, HD 141569, was unresolved at all wavelengths between 2.0 and 2.4 μm, indicating a lack of dust or gas in the inner disk regions. Another target, VV Ser, was overresolved, indicating that the emission spans angles larger than $\sim$5 mas at all observed wavelengths.

The near-IR emission from the remaining targets was resolved, and our data show that the angular size of the near-IR emission increases with wavelength in all cases. This behavior suggests temperature gradients in these inner disks, arising from the combination of warm dust at its sublimation temperature and hotter, presumably gaseous material within the dust sublimation radius. Our data clearly indicate emission from the Brγ transition of hydrogen in several objects, and suggest that water vapor and carbon monoxide gas are present in the inner disks of some targets.

We constructed simple physical models of the inner disk, including dust and gas emission, and we fitted them to our data to constrain the spatial distribution and temperature of dust and gas emission components. We considered models including only dust emission; dust, gas continuum, and Brγ emission; and dust, gas continuum, water vapor, and Brγ emission. Models incorporating only dust emission cannot fit the data for any of our sources well. In contrast, models including dust and gas emission are suitable for explaining our data. The inclusion or exclusion of water vapor in these dust + gas models did not substantially affect the quality of the fits in most cases.

For all sources where Brγ emission is observed, we find it to be compact relative to the continuum emission. This contrasts with previous findings, which found Brγ emission to be extended relative to the continuum around some high-mass stars. The results presented here suggest that Brγ commonly traces infalling material around young stars spanning a large range in stellar mass.

CO emission is tentatively observed toward several objects, and we see evidence that this emission has a more compact spatial distribution than the dust around RW Aur. For other objects, our data are insufficient to place meaningful constraints on the relative spatial distribution of CO and other emission components. We will reobserve these targets in the near future with higher dispersion, to obtain better signal-to-noise for the relatively narrow CO lines and better constrain their spatial distribution.

While models including water vapor opacity often fit our data well, the best-fit models generally also require continuum emission from material that is too hot to be water (since water dissociates at $\sim$3000 K). We do not have a ready explanation for the source of this hot continuum emission, but we speculate that it may trace free–free emission from hydrogen and/or H$^-$. The gas densities and fractional ionizations required to produce such emission seem plausible in the inner regions of protoplanetary disks, suggesting that free–free emission from H and H$^-$ is a viable explanation for the compact continuum emission seen in our data.

Data presented herein were obtained at the W. M. Keck Observatory, in part from telescope time allocated to the National Aeronautics and Space Administration through the agency's scientific partnership with Caltech and the University of California. The Observatory was made possible by the

generous financial support of the W. M. Keck Foundation. The authors recognize and acknowledge the cultural role and reverence that the summit of Mauna Kea has always had within the indigenous Hawaiian community. We are most fortunate to have the opportunity to conduct observations from this mountain. This work has used software from the Michelson Science Center at Caltech. The authors thank the entire KI team for making these observations possible. We also thank the referee, Geoff Blake, for his thoughtful and detailed referee report, which greatly improved the manuscript.

REFERENCES

Akeson, R. L., et al. 2005a, ApJ, 635, 1173
Akeson, R. L., et al. 2005b, ApJ, 622, 440
Bell, K. L., & Berrington, K. A. 1987, J. Phys. B: At. Mol. Opt. Phys., 20, 801
Berthoud, M. G. 2008, PhD thesis, Cornell Univ.
Bertout, C., Basri, G., & Bouvier, J. 1988, ApJ, 330, 350
Blake, G. A., & Boogert, A. C. A. 2004, ApJ, 606, L73
Boden, A. F., Colavita, M. M., van Belle, G. T., & Shao, M. 1998, in Proc. SPIE 3350, Astronomical Interferometry, ed. R. D. Reasenberg (Bellingham, WA: SPIE), 872
Brittain, S. D., Simon, T., Najita, J. R., & Rettig, T. W. 2007, ApJ, 659, 685
Calvet, N., Hartmann, L., & Kenyon, S. J. 1991, ApJ, 383, 752
Carr, J. S. 1989, ApJ, 345, 522
Carr, J. S., Tokunaga, A. T., & Najita, J. 2004, ApJ, 603, 213
Chandrasekhar, S., & Breen, F. H. 1946, ApJ, 104, 430
Chiang, E. I., & Goldreich, P. 1997, ApJ, 490, 368
Colavita, M., et al. 2003, ApJ, 592, L83
Colavita, M. M. 1999, PASP, 111, 111
Colavita, M. M., & Wizinowich, P. L. 2003, in Proc. SPIE 4838, Interferometry for Optical Astronomy II, ed. W. A. Traub (Bellingham, WA: SPIE), 79
Cutri, R. M., et al. 2003, 2MASS All Sky Catalog of point sources (The IRSA 2MASS All-Sky Point Source Catalog NASA/IPAC Infrared Science Archive) http://irsa.ipac.caltech.edu/applications/Gator/
Dullemond, C. P., Dominik, C., & Natta, A. 2001, ApJ, 560, 957
Dullemond, C. P., van den Ancker, M. E., Acke, B., & van Boekel, R. 2003, ApJ, 594, L47
Eiroa, C., et al. 2002, A&A, 384, 1038
Eisner, J. A. 2007, Nature, 447, 562
Eisner, J. A., Chiang, E. I., Lane, B. F., & Akeson, R. L. 2007a, ApJ, 657, 347
Eisner, J. A., Hillenbrand, L. A., White, R. J., Akeson, R. L., & Sargent, A. I. 2005, ApJ, 623, 952
Eisner, J. A., Hillenbrand, L. A., White, R. J., Bloom, J. S., Akeson, R. L., & Blake, C. H. 2007c, ApJ, 669, 1072
Eisner, J. A., Lane, B. F., Akeson, R. L., Hillenbrand, L., & Sargent, A. 2003, ApJ, 588, 360
Eisner, J. A., Lane, B. F., Hillenbrand, L., Akeson, R., & Sargent, A. 2004, ApJ, 613, 1049
Eisner, J. A., et al. 2007b, ApJ, 654, L77
Folha, D. F. M., & Emerson, J. P. 2001, A&A, 365, 90
Garcia Lopez, R., Natta, A., Testi, L., & Habart, E. 2006, A&A, 459, 837
Glass, I. S., & Penston, M. V. 1974, MNRAS, 167, 237
Gorti, U., & Hollenbach, D. 2004, ApJ, 613, 424
Goto, M., Usuda, T., Dullemond, C. P., Henning, T., Linz, H., Stecklum, B., & Suto, H. 2006, ApJ, 652, 758
Gray, D. F. 1992, The Observation and Analysis of Stellar Photospheres (Cambridge: Cambridge Univ. Press)
Greene, T. P., & Lada, C. J. 1996, AJ, 112, 2184
Herbig, G. H., & Bell, K. R. 1988, Lick Observatory Bulletin (Santa Cruz, CA: Lick Observatory)
Herbst, W., & Shevchenko, V. S. 1999, AJ, 118, 1043
Hillenbrand, L. A., Strom, S. E., Vrba, F. J., & Keene, J. 1992, ApJ, 397, 613
Isella, A., & Natta, A. 2005, A&A, 438, 899
Isella, A., Tatulli, E., Natta, A., & Testi, L. 2008, A&A, 483, L13
Jensen, E. L. N., & Mathieu, R. D. 1997, AJ, 114, 301
John, T. L. 1988, A&A, 193, 189
Kenyon, S. J., & Hartmann, L. 1995, ApJS, 101, 117
Koresko, C. D. 2002, AJ, 124, 1082
Kraus, S., Preibisch, T., & Ohnaka, K. 2008, ApJ, 676, 490
Lada, C. J., & Adams, F. C. 1992, ApJ, 393, 278
Lewis, J. S. 1997, Physics and Chemistry of the Solar System (rev. ed.; San Diego, CA: Academic Press)
Ludwig, C. B. 1971, Appl. Opt., 10, 1057
Malbet, F., et al. 2007, A&A, 464, 43
Malfait, K., Bogaert, E., & Waelkens, C. 1998, A&A, 331, 211
Mandell, A. M., Mumma, M. J., Blake, G. A., Bonev, B. P., Villanueva, G. L., & Salyk, C. 2008, ApJ, 681, L25
Marcy, G., Butler, R. P., Fischer, D., Vogt, S., Wright, J. T., Tinney, C. G., & Jones, H. R. A. 2005, Prog. Theor. Phys. Suppl., 158, 24
Mendoza, E. E. 1966, ApJ, 143, 1010
Mendoza, E. E. 1968, ApJ, 151, 977
Millan-Gabet, R., Malbet, F., Akeson, R., Leinert, C., Monnier, J., & Waters, R. 2007, in Protostars and Planets V, ed. B. Reipurth, D. Jewitt, & K. Keil (Tucson, AZ: Univ. Arizona Press), 539
Millan-Gabet, R., Schloerb, F. P., & Traub, W. A. 2001, ApJ, 546, 358
Monnier, J. D., et al. 2005, ApJ, 624, 832
Monnier, J. D., et al. 2006, ApJ, 647, 444
Muzerolle, J., Calvet, N., Hartmann, L., & D'Alessio, P. 2003, ApJ, 597, L865
Muzerolle, J., D'Alessio, P., Calvet, N., & Hartmann, L. 2004, ApJ, 617, 406
Najita, J., Carr, J. S., Glassgold, A. E., Shu, F. H., & Tokunaga, A. T. 1996a, ApJ, 462, 919
Najita, J., Carr, J. S., & Mathieu, R. D. 2003, ApJ, 589, 931
Najita, J., Carr, J. S., & Tokunaga, A. T. 1996b, ApJ, 456, 292
Najita, J. R., Carr, J. S., Glassgold, A. E., & Valenti, J. A. 2007, in Protostars and Planets V, ed. B. Reipurth, D. Jewitt, & K. Keil (Tucson, AZ: Univ. Arizona Press), 951, 507
Najita, J. R., Doppmann, G., Carr, J. S., Graham, J., & Eisner, J., ApJ, 2009, in press
Najita, J. R., Edwards, S., Basri, G., & Carr, J. 2000, in Protostars and Planets, IV, ed. V. Mannings, A. P. Boss, & S. S. Russell (Tucson, AZ: Univ. of Arizona Press), 457
Perryman, M. A. C., et al. 1997, A&A, 323, L49
Pollack, J. B., Hollenbach, D., Beckwith, S., Simonelli, D. P., Roush, T., & Fong, W. 1994, ApJ, 421, 615
Pontoppidan, K. M., Blake, G. A., van Dishoeck, E. F., Smette, A., Ireland, M. J., & Brown, J. 2008, ApJ, 684, 1323
Pontoppidan, K. M., Dullemond, C. P., Blake, G. A., Boogert, A. C. A., van Dishoeck, E. F., Evans, N. J. II, Kessler-Silacci, J., & Lahuis, F. 2007, ApJ, 656, 980
Prato, L., Greene, T. P., & Simon, M. 2003, ApJ, 584, 853
Salyk, C., Pontoppidan, K. M., Blake, G. A., Lahuis, F., van Dishoeck, E. F., & Evans, N. J., II. 2008, ApJ, 676, L49
Shu, F., Najita, J., Ostriker, E., Wilkin, F., Ruden, S., & Lizano, S. 1994, ApJ, 429, 781
Skrutskie, M. F., Meyer, M. R., Whalen, D., & Hamilton, C. 1996, AJ, 112, 2168
Steenman, H., & Thé, P. S. 1991, Ap&SS, 184, 9
Tannirkulam, A., et al. 2008, ApJ, 677, L51
Tatulli, E., et al. 2007, A&A, 464, 55
Thi, W.-F., & Bik, A. 2005, A&A, 438, 557
Weidenschilling, S. J. 1977, Ap&SS, 51, 153
White, R. J., & Ghez, A. M. 2001, ApJ, 556, 265